Process Optimization of Dual-Laser Beam Welding of Advanced Al-Li Alloys Through Hot Cracking Susceptibility Modeling

YINGTAO TIAN, JOSEPH D. ROBSON, STEFAN RIEKEHR, NIKOLAI KASHAEV, LI WANG, TRISTAN LOWE, and ALEXANDRA KARANIKA

Laser welding of advanced Al-Li alloys has been developed to meet the increasing demand for light-weight and high-strength aerospace structures. However, welding of high-strength Al-Li alloys can be problematic due to the tendency for hot cracking. Finding suitable welding parameters and filler material for this combination currently requires extensive and costly trial and error experimentation. The present work describes a novel coupled model to predict hot crack susceptibility (HCS) in Al-Li welds. Such a model can be used to shortcut the weld development process. The coupled model combines finite element process simulation with a two-level HCS model. The finite element process model predicts thermal field data for the subsequent HCS hot cracking prediction. The model can be used to predict the influences of filler wire composition and welding parameters on HCS. The modeling results have been validated by comparing predictions with results from fully instrumented laser welds performed under a range of process parameters and analyzed using high-resolution X-ray tomography to identify weld defects. It is shown that the model is capable of accurately predicting the thermal field around the weld and the trend of HCS as a function of process parameters.

I. INTRODUCTION

THE newly developed lithium-bearing 2xxx series aluminum alloys have shown great potential for aerospace applications due to their high specific strength plus high stiffness. It is known that every 1 pct (wt) of lithium blended into aluminum increases the elastic modulus by about 6 pct and reduces the density by about 3 pct at the same time.[1] The recently developed Li-bearing AA2198 and AA2196 aluminum alloys are very promising high-strength and light-weight alloys for aircraft manufacturing, for example, the skin-stringer T-shaped joints for fuselage panels. There is a strong motivation in the aerospace industry to use laser beam welding to manufacture skin-stringer structures due to the weight saving by replacing the traditional riveted structure with a welded component. However, Li-bearing aluminum alloys typically present severe weldability issues of high hot cracking susceptibility (HCS) in the joints.[1–4] Hot cracking, also referred as hot tearing or hot shortness, occurs during the solidification of the welding pool in the temperature range above solidus, which can cause a failure of the joint immediately after welding or initiate a fatigue crack during the service. Therefore, understanding and minimizing hot cracking is critical to achieving good quality joints. At present, the only way to find a set of processing parameters and weld filler chemistry that avoids hot cracking is through trial and error experimentation. This is inefficient with no guarantee that an optimum parameter set will be deduced. There is thus a strong motivation to develop a simulation tool that can predict HCS and guide the selection of the best parameters for welding. Furthermore, a physics-based model can help in understanding the factors that contribute to hot cracking, and thus guide future alloy and filler wire development. The objective of the present work was to develop a physics-based model to predict HCS in Al-Li laser welds and validate the model against results from experimental welds performed under a range of conditions.

Hot cracking models in the literature have typically been developed to predict HCS in castings. Since casting and welding both involve liquid metal solidification, such models can be adapted to deal with HCS in welds. The most successful of these models for application to aluminum alloys is that developed by Rappaz, Drezet, and Gremaud (RDG).[5] This is a physics-based model that attempts to capture all of the key processes that lead to hot cracking. This model has been validated in a number of aluminum alloy systems.[6–10]

YINGTAO TIAN and LI WANG, Research Associates, and JOSEPH D. ROBSON, Professor, are with School of Materials, The University of Manchester, M13 9PL, Manchester, UK. Contact e-mail: yingtao.tian@manchester.ac.uk STEFAN RIEKEHR, Materials Scientist, and NIKOLAI KASHAEV, Head of Department, are with the Institute of Materials Research, Materials Mechanics, Helmholtz-Zentrum Geesthacht, Max-Planck-Str. 1, 21502 Geesthacht, Germany. TRISTAN LOWE, Experimental Officer, is with Henry Mosely X-ray Imaging Facility, School of Materials, University of Manchester, Manchester, UK. ALEXANDRA KARANIKA, Project Leader, is with Research and Product Design, Hellenic Aerospace Industry S.A., P.O. Box 23, 32009 Schimatari, Greece.
Manuscript submitted December 14, 2015.
Article published online April 20, 2016

The RDG model attributes the formation of hot cracking to two main factors: lack of liquid feeding; and tensile deformation in the coherent dendritic network caused by thermal contraction of the solid. This model is based on the observation that hot cracking occurs in the vulnerable mushy zone when the material is at a temperature between the coherency temperature and solidus. The coherency temperature is defined as the point when the solid dendritic arms coalesce so that they can sustain and transmit stresses. Above the coherency temperature, the liquid phase between the dendritic arms is still continuous and the solid is usually considered as slurry, so no hot cracking occurs at this stage. Once the temperature drops below the coherency temperature, the thermal stress, which is induced by the differential thermal contraction upon cooling, can pull apart the weakly coalesced dendritic arms and provide a potential site for hot cracking. If enough liquid is able to flow into such regions, the potential hot crack is 'healed' and a crack will not form. However, if the permeability of the mushy zone is too small to allow enough liquid feeding into the space, then the hot cracking occurs. The RDG model combines the feeding of the liquid into the mushy zone and the deformation of the coherent solid network and also offers a strain rate-based criterion to work out the relative probability of hot tears. The RDG model thus includes all of the important phenomena that lead to hot cracking, while retaining an analytical framework that does not require knowledge of the distribution of dendrites and liquid in space. This model was not originally developed for welding, but has been successfully applied to predict hot crack susceptibility in 6xxx aluminum alloy welds.[11]

In the present work, a coupled model is developed to address the hot cracking issues in laser welding of the newly developed Al-Li alloys. A finite element (FE) model is developed to simulate the dual-beam laser welding processes and predict the thermal field data which feed into the RDG hot cracking susceptibility (HCS) model. The RDG hot cracking model was chosen since it has proven successful in predicting hot cracking in other aluminum alloys that are susceptible to cracking during welding.[11]

To validate the model, dual-beam laser welding of AA2198 skin (sheet) to AA2196 stringer (extrusion) has been studied under a range of process conditions. The predictions of the model have been compared with the tendency for hot cracks in the experimental welds measured using X-ray computed tomography (XCT). The use of XCT to study hot cracks and other defects in Al-Li alloy laser welds performed under a range of conditions is also a novel aspect of the present work.

II. EXPERIMENTAL METHOD

Welding was performed using the large-scale laser welding facility at Helmholtz–Zentrum Geesthacht (HZG), Germany. The facility consists of a movable processing head and two 3.5 kW CO_2 laser units. The skin-stringer T-shaped welded joint comprises three materials, AA2198 as the skin, AA2196 as the stringer, and AA4047 as the filler. The materials were supplied by Constellium and the nominal compositions are listed in Table I. As shown in Figures 1(a) and (b), the 3.2-mm-thick skin sheet was vacuum clamped onto an aluminum base while the extruded profile stringer was placed vertically and held in place with good contact. The presence of lithium element in the alloys increases the growth rate of the oxide film on the surface, which is mainly responsible for the formation of porosity during the welding. Therefore, extra attention needs to be paid to prepare the surface before welding. The surface of the skin material was ground with sand paper to remove the oxide layer. It has been found that the oxide layer on AA2196 contains higher hydrogen level, so that the surface of the stringer AA2196 was ground down to at least 0.2 mm. The final thickness of stringer after surface preparation was 1.6 mm. AA4047 filler wire with a diameter of 0.8 mm was used.

Details of the dual-laser beam welding parameters are listed in Table II. Two CO_2 laser beams were applied simultaneously on both sides of the stringer at a fixed incident angle of 22 deg, respectively. The filler wire was fed at 7.0 m/min and helium shielding gas was supplied at a flow rate of 35 L/min in front of the laser beam on both sides of the stringer. The focal position of the laser beam was 0.0 mm on the stringer surface and +0.2 mm above the skin. Three welding experiments were carried out for comparison. Due to the restriction of the equipment and requirement of high productivity, the welding speed, filler wire feed rate, He gas flow, and laser focal position remained same but laser power varied from 1400 to 2000 W. In order to reveal the micro-cracks, the welds were sectioned out (Figure 1(c)) and examined in a Nikon XTH-225 high-resolution X-ray tomographic system at the Henry Moseley X-ray Imaging Facility. The excessive parent materials were removed to enable better accessibility of X-ray to the region of greatest interests, i.e., the fusion zone, and about 1-cm-long section from the middle of each weld was examined. The sample was rotated through 360 deg and an accelerating voltage of 105 kV and a 120 μA current were used to produce a total of 2002 radiographs with a voxel size of 5 μm, i.e., features larger than 5 μm will be recognized by the system. The radiographic data were reconstructed using CT Pro 3D (version XTEK XT 4.0.3.6). The defects in the welds were finally segmented

Table I. Nominal Chemical Composition (Weight Percent) of the Three Aluminum Alloys

Material	Si	Fe	Cu	Mn	Mg	Cr	Zn	Ti	Ag	Li	Zr	Al
AA2198	0.03	0.05	3.35	0.03	0.32	0.05	0.02	0.02	0.27	0.98	0.14	bal.
AA2196	0.03	0.05	3.03	0.31	0.37	0.01	0.02	0.03	0.26	1.74	0.11	bal.
AA4047	12.0	0.8	0.3	0.15	0.1	—	0.2	—	—	—	—	bal.

(a)

Stringer
Shielding gas
Filler wire
Laser beam
Skin

α

(b)

6 mm

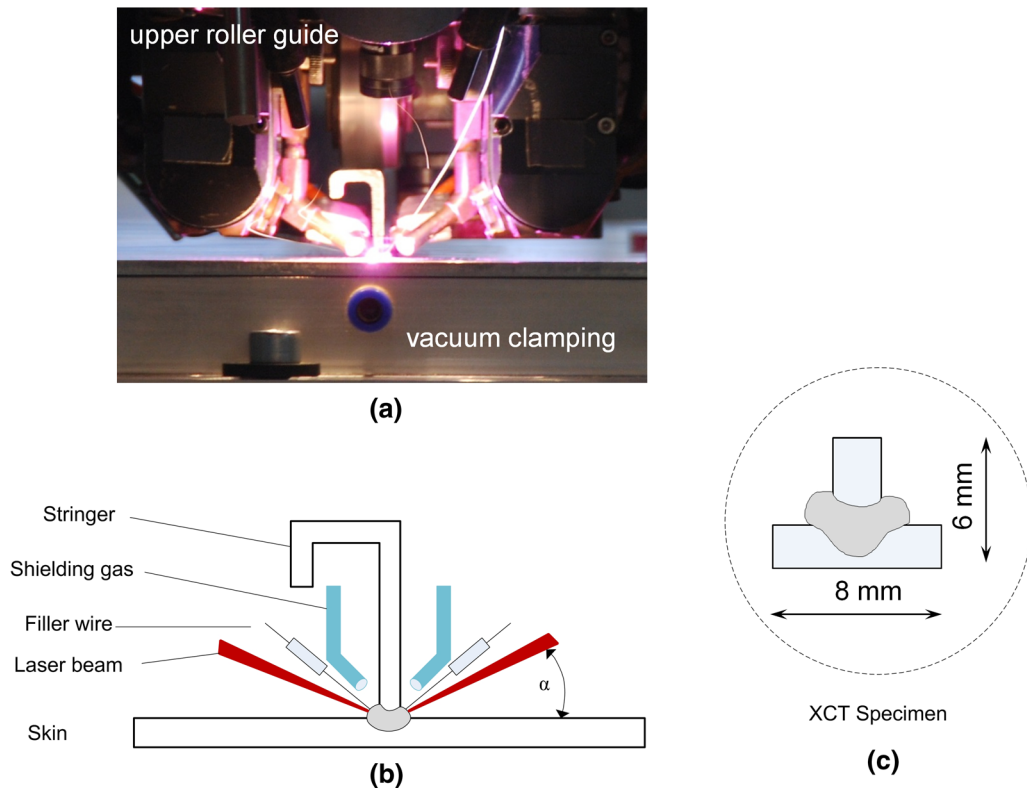8 mm

XCT Specimen

(c)

Fig. 1—Configuration of the laser welding skin-stringer process and X-ray CT sample.

Table II. Details of Dual-Beam Laser Welding Parameters

Laser Power	Welding Speed	Filler Wire Feed Rate	He Gas Flow Rate	Incident Angle (α)	Focal Position	Beam Focus Diameter
1400/1700/2000 W	6.2 m/min	7.0 m/min	35 L/min	22 deg	0.0 mm	130 μm

and visualized using FEI Avizo 9.1 visualization package.

III. WELDING PROCESS AND HOT CRACKING SUSCEPTIBILITY MODEL DESCRIPTION

A. Finite Element Analysis Procedure

ABAQUS was used as a general modeling tool in this study. However, in order to model multiple moving heat sources directly in ABAQUS, a complex FORTRAN subroutine is required. In this work, another finite element analysis software, namely the Finite Element Analysis Toolbox (FEAT), was utilized to define the heat source and apply it into the ABAQUS model. FEAT incorporates a powerful Welding Modeling Toolbox (WMT), with the moving heat source function integrated, to perform accurate welding thermal and stress/strain modeling. By combining the advantages of ABAQUS and FEAT-WMT, a new modeling procedure was adopted. The geometric model was firstly created in ABAQUS and the material properties, boundary conditions, meshing, welding, and cooling time were defined. The only thing absent in this stage was the thermal load. An '.inp' file containing complete information for the model was generated. As designed, FEAT-WMT can read the ABAQUS '.inp' file to simulate the heat source. The heat source is described in Section III–B. The heat source was defined in FEAT-WMT using the built-in templates and applied into the 3D model read from ABAQUS. FEAT-WMT then generated a series of SLICE files which contained the information of the moving heat source. Next, the 'inp' file and SLICE files generated from the previous steps were read into ABAQUS again. The SLICE files were organized by a simple FORTRAN subroutine and simulated the moving heat source in ABAQUS. The thermal analysis was then carried out in ABAQUS using the standard solver.

B. Heat Source Model

An elliptic cone heat source, which was derived from the classic Goldak double ellipsoid model,[12] was used to simulate the temperature field during the dual-beam

laser welding process. The Goldak double ellipsoid model has been successfully applied to arc welding process but it is not suitable to simulate the deep keyhole during laser penetration welding. As shown in Figure 2, the elliptic cone has the Gaussian distribution in the X–Z plane (same as the Goldak double ellipsoid distribution), but has a linear variation in the Y direction down into the material.[13] Similar to the Goldak double ellipsoid model, the heat source is divided into front and rear parts. The front part of the double elliptic cone is defined as:

$$q_f(x,y,z) = \frac{6f_f Q}{abc_f \pi (1+d_c)} \exp\left(-3\frac{x^2}{a^2}\right) \\ \times \left[1 - \frac{(1-d_c)|y|}{b}\right] \exp\left(-3\frac{z^2}{c_f^2}\right) \quad [1]$$

and the rear part as:

$$q_r(x,y,z) = \frac{6f_r Q}{abc_r \pi (1+d_c)} \exp\left(-3\frac{x^2}{a^2}\right) \\ \times \left[1 - \frac{(1-d_c)|y|}{b}\right] \exp\left(-3\frac{z^2}{c_r^2}\right), \quad [2]$$

where Q is the energy input, a, c_f, and c_r are the lateral, front, and rear radius of the ellipsoid on the X–Z plane, respectively, b is the depth of the blunt cone. The parameters f_f and f_r are the fractions between the front and rear parts in the conical functions, respectively. To keep continuity between the front and rear parts of the combined heat source, the following relationships must be satisfied:

$$\begin{cases} f_f = \dfrac{2c_f}{c_f + c_r} \\ f_f + f_r = 2 \end{cases} \quad [3]$$

The geometric parameters a, c_r, and c_f determine the area of the top surface of the heat source and the parameter b defines how deep the laser penetrates into the material. The additional parameter d_c defines the fraction of energy intensity decrease through the length of b. d_c is a normalized parameter and has a value between 1 and 0. If the value of d_c is 1, the energy

intensity is constant from the top to the bottom of the cone, while $d_c = 0$ means the energy intensity decreases to zero at the bottom of the weld. This model therefore allows manipulation of the key features of the heat source to accurately simulate the laser welding process.

C. Welding Process Model Configuration

The weld specimens were 310 mm long, corresponding to a 3-second welding time. Simulations showed that welding will enter steady state soon after the starting point, so it is sensible to reduce the length of the weld to 100 mm in the model to save computing time and resources. An example weld and the 3D model are shown in Figure 3. Note that the meshes are significantly refined near the weld, where the temperature changes rapidly. The volume of the weld bead was calculated from the filler wire feed rate, which was predefined in the model. The material properties were supplied by Constellium and are listed in Table III. It is assumed that the materials are continuous and the temperature dependency of the thermal conductivity and specific heat are accounted (see Table III). The latent heat due to the solid–liquid phase transformation in three materials was also considered. The heat loss through radiation, surface convection, and conduction to the backing plate and clamps were set up according to the experimental conditions. The typical value of heat transfer coefficient between work piece and air is around 10 Wm^{-2} K^{-1}.[14] In order to simulate the reinforced heat transfer induced by the helium shielding gas, backing plate, and clamping, the heat transfer coefficient for surfaces near the weld, on the backside, and between the clamping were artificially increased, as listed in Table IV.

D. Welding Process Model Optimization and Validation

To optimize and verify the accuracy of the thermal model, a number of thermocouples were attached to the skin and stringer (Figure 4) and the measured results were compared with the simulation. The area and profile of the fusion zone in the welds were also measured from a cross-sectional view and compared with the simulation results. The geometrical characteristics of the heat source Eqs. [1] and [2], the heat transfer coefficient and the boundary conditions were adjusted to fit the measured temperature and profile of fusion zones. The model was therefore adjusted and optimized on the basis of the comparison.

E. The Hot Cracking Susceptibility Model

As already discussed, when the coherent dendrites are subjected to a tensile strain rate and the liquid flowing into the gaps cannot compensate for the deformation, hot cracking will occur. The RDG model is derived by performing a mass balance over a local region of the mushy zone and it can be applied in either a simple way to obtain a qualitative ranking of HCS, or in a more complex way to provide quantitative prediction of hot crack formation. Details of the RDG model derivation can be found in Reference 5.
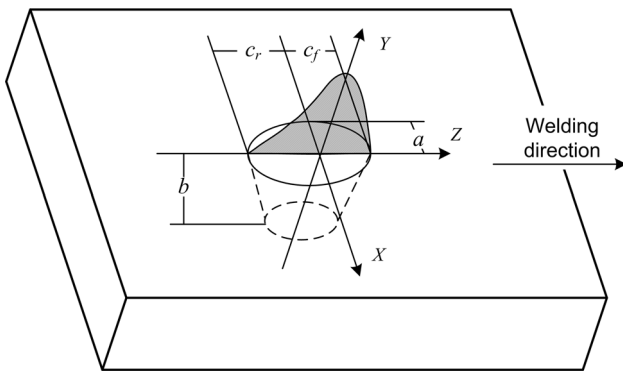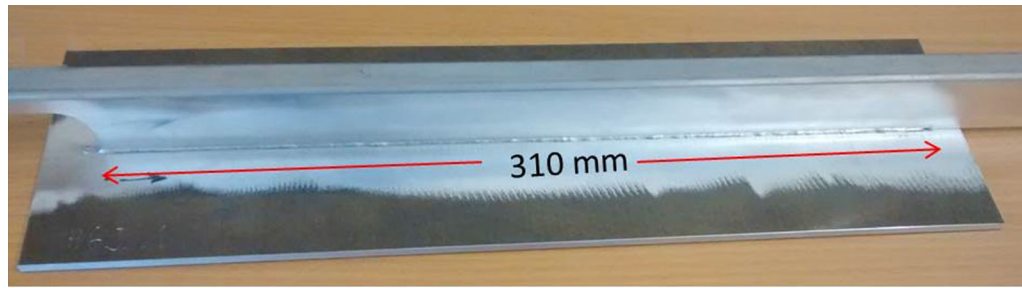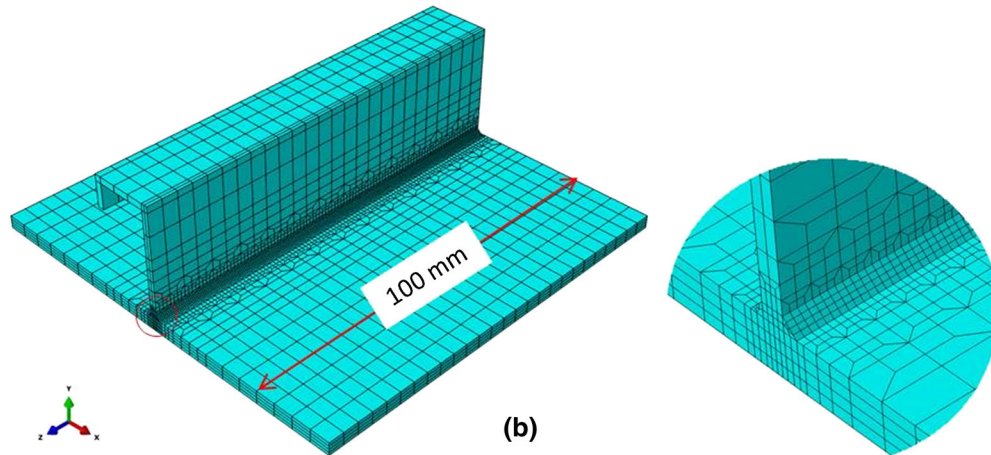

Fig. 2—Configuration of the elliptic cone heat source.

(a)

(b)

Fig. 3—The actual welding specimen (*a*) and 3D model in ABAQUS (*b*) (Color figure online).

Table III. Thermodynamic Properties of AA2198, AA2196, and AA4047 Aluminum Alloys

Alloys	Temperature [K (°C)]	293 (20)	323 (50)	423 (150)	523 (250)	623 (350)	723 (450)
AA2198	density (k gm^{-3})	2690	2684	2664	2642	2619	2594
	thermal conductivity (Wm^{-2} K^{-1})	85	92	111	123	131	136
	specific heat (Jkg^{-1} K^{-1})	903	922	975	1019	1059	1101
	latent heat for fusion (J/kg)				407000		
	melting temperature range (K)				776–923		
AA2196	density (kg m^{-3})	2638	2632	2611	2590	2566	2541
	thermal conductivity	66	72	90	102	110	117
	specific heat (J kg^{-1} K^{-1})	921	941	997	1041	1081	1123
	latent heat for fusion (J/kg)				410000		
	melting temperature range (K)				781–921		
AA4047	density (kg m^{-3})	2659	2654	2637	2619	2600	2579
	thermal conductivity	173	179	193	197	197	197
	specific heat (J kg^{-1} K^{-1})	871	891	943	985	1026	1067
	latent heat for fusion (J/kg)				490000		
	melting temperature range (K)				808–858		

Table IV. Numerical Parameters of Heat Loss to Environment

Emissivity	0.4
Surface convective heat transfer coefficient (Wm^{-2} K^{-1})	10
Forced convective heat transfer near the weld induced by shielding gas (Wm^{-2} K^{-1})	80
Effective forced heat transfer induced by backing plate and clamping (Wm^{-2} K^{-1})	100

The simplest application of this model is to rank the relative sensitivity to hot cracking for different alloy and filler metal compositions. As shown in Figure 5, when the pressure in the inter-dendritic liquid (p_m) drops below a critical level, called cavitation pressure (p_c), the liquid is unable to refill the gaps and therefore a hot crack may form. The pressure drop through the dendrite network has two components, Δp_{sh} is caused by the solidification shrinkage and Δp_s is due to the deformation, as expressed below.
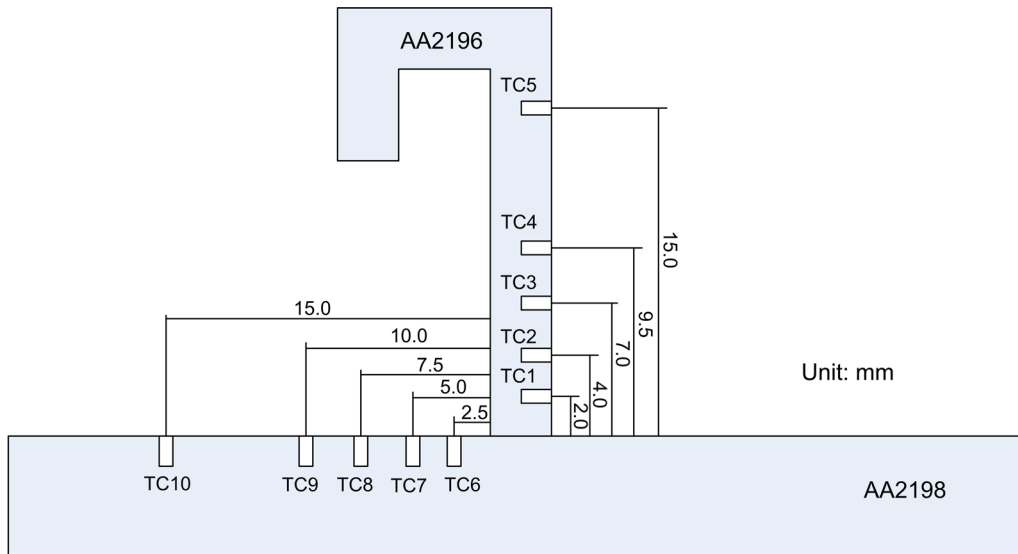
Fig. 4—Positions of the thermocouples (TC) embedded in skin and stringer during laser welding.
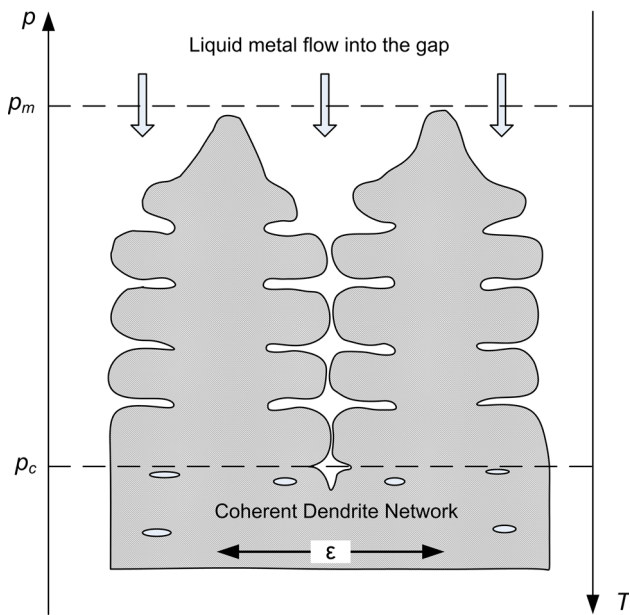

Fig. 5—Schematics of the occurrence of hot cracking between dendrite networks.[5]

$$\Delta p_{\mathrm{max}} = p_{\mathrm{m}} - p_{\mathrm{c}} = \Delta p_{\mathrm{c}} = \Delta p_{\mathrm{sh}} + \Delta p_{\varepsilon}$$

$$= \frac{180}{\lambda_2^2} \frac{v_T \beta \mu}{G} A + \frac{180}{\lambda_2^2} \frac{(1+\beta)\mu\dot{\varepsilon}(T)}{G^2} B \qquad [4]$$

with

$$A = \int_{T_s}^{T_l} \frac{f_s(T)^2}{(1 - f_s(T))^2} \mathrm{d}T \qquad [5]$$

$$B = \int_{T_s}^{T_l} \frac{f_s(T)^2 \int_{T_s}^{T_l} f_s(T) \mathrm{d}T}{(1 - f_s(T))^3} \mathrm{d}T, \qquad [6]$$

where λ_2 is the secondary dendrite arm spacing, G is the thermal gradient, v_T is the velocity of the isotherms, β is the shrinkage factor, μ is the liquid viscosity, and $f_s(T)$ is the solid fraction dependent on temperature. The first term on the right-hand side of Eq. [4] is related to the microporosity induced by the solidification shrinkage while the second term relates to the deformation.

The two integrals A and B can be used as an index to evaluate the relative hot cracking susceptibility. The larger A and B, the larger the pressure drop in the inter-dendritic liquid and therefore the higher risk of hot cracking. A and B are solely dependent on the fraction of solid $f_s(T)$ during solidification as a function of temperature. It is commonly assumed that the dendrites start to bridge together when the solid fraction reaches approximately 98 pct if the eutectic temperature is not yet reached.[5,15,16] Therefore, the integral limits for the A parameter in Eq. [5] are from the point where the solid fraction $f_s = 0.98$, i.e., the so-called coherency temperature, to the liquidus temperature. The temperature-dependent fraction of solid can be determined from a thermodynamic calculation alone, using the Scheil–Gulliver assumption, which is known to well represent the solidification of aluminum alloys under standard conditions.[17] This application of the RDG model is therefore only dependent on fusion zone composition (which depends on base metal and filler composition, and the proportion of each in the melt pool). In the present work, JMatPro[18] with the ALDATA database was used to perform the thermodynamic calculations to determine A and B parameters.

A more complete application of the RDG model also includes a consideration of the welding process. By including factors such as the isotherm velocity, the model will be able to determine the maximum strain rate that can be sustained in the mushy zone. Equation [4] can be rearranged to give this strain rate as:
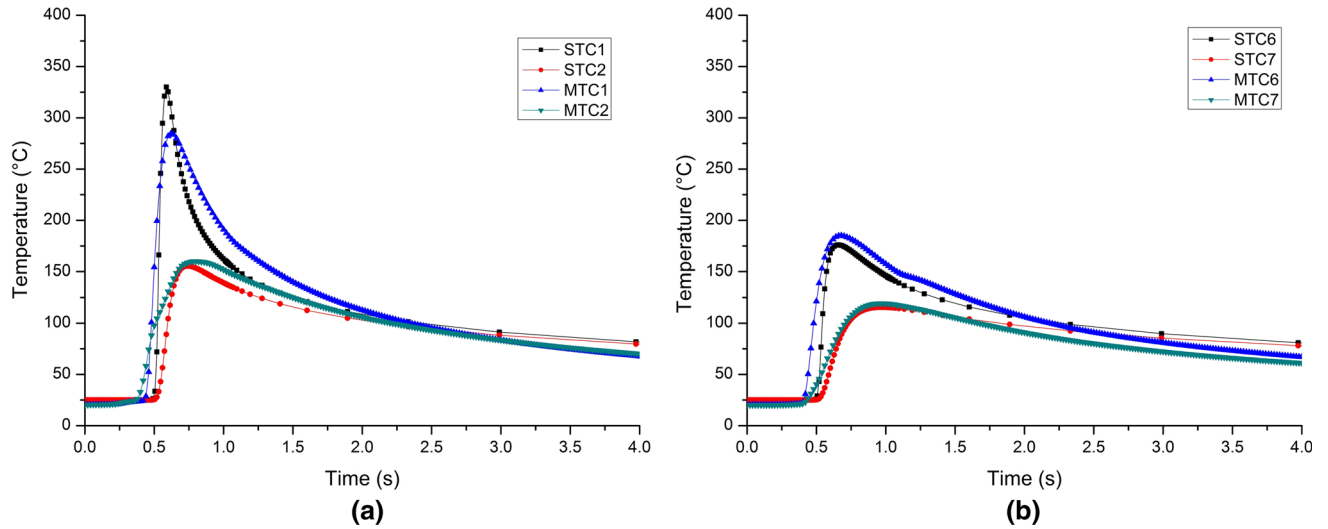
Fig. 6—Comparison of simulated and measured temperature at certain thermocouple planted on stringer (*a*) and skin (*b*) for 2000 W laser welding process. STC—simulated thermocouple temperature; MTC—measured thermocouple temperature.

Table V.   Differences on Peak Temperatures at Thermocouple Positions Between Measurement and Simulation

Thermocouples	Measured Peak Temperature [K (°C)]	Simulated Peak Temperature [K (°C)]	Difference [K (°C)]	RMS Error
TC1	558 (285)	602 (329)	+44 (+44)	9.25 pct
TC2	433 (160)	429 (156)	−4 (−4)	
TC6	458 (185)	449 (176)	−9 (−9)	
TC7	393 (120)	389 (116)	−4 (−4)	

$$\dot{\varepsilon}_{p,\max} = \frac{\lambda_2^2}{180} \frac{G}{(1+\beta)\mu} \Delta p_c - v_T \frac{\beta}{1+\beta} A, \qquad [7]$$

where Δp_c is the cavitation depression. The HCS index is then assumed to be proportional to $1/\dot{\varepsilon}_{p,\max}$, *i.e.*, the higher strain rate the mushy zone can bear, the lower risk of hot cracking. The second-level criterion allows the influences of both thermal field and the alloy composition to be included in the calculation. To perform the calculation using Eq. [7], the thermal gradient G was obtained through the aforementioned finite element thermal model. The secondary dendrite arm spacing λ_2 was calculated using JMatPro, while values for other variables were taken from Reference 5.

IV.   RESULTS AND DISCUSSION

A. *Thermal Modeling Results and Discussion*

Thermal analyses of the dual-laser beam welding processes were conducted using ABAQUS and FEAT-WMT for various parameters listed in Table II. Figure 6 compares the measured and simulated temperatures at the thermocouple placed on stringer and skin, respectively for 2000 W dual-laser welding process. In order to present the data clearly, only data from the four thermocouples close to the welds are shown in the

diagram. The accuracy of the prediction is evaluated by the root mean square (RMS) error, which is presented as:

$$\text{Error}_{\text{RMS}} = \sqrt{\sum_1^4 \frac{1}{4} \left\{ \frac{(\theta_{\text{TCn,peak}} - \theta_{\text{TCn},0})}{\Delta\theta_{\text{TCn,mean}}} \right\}^2}, \qquad [8]$$

where $\theta_{\text{TCn,peak}}$ is the peak temperature predicted at thermocouple TCn, $\theta_{\text{TCn},0}$ is the initial temperature at TCn, $\theta_{\text{TCn,mean}}$ is the mean of the temperature rise measured in experiment at TCn. The RMS error for the temperature prediction shown in Figure 6 is below 10 pct. As expected, TC1 thermocouple records the highest temperature in both measured and simulated cases as it is the closest to the weld center. The peak temperature measured by TC1 was 558 K (285 °C), while the peak predicted temperature was 602 K (329 °C). This error was larger than that of any of the other thermocouple positions (Table V). Most important however is correct prediction of the fusion zone boundary, since this calculation is required to predict the melt pool composition, and hence HCS. The simulated fusion zone and fusion boundary are compared in Figure 7. Figure 8 compares the fusion zone area as a function of power level. These results show that the model provides a very good prediction of both the fusion zone shape and area.
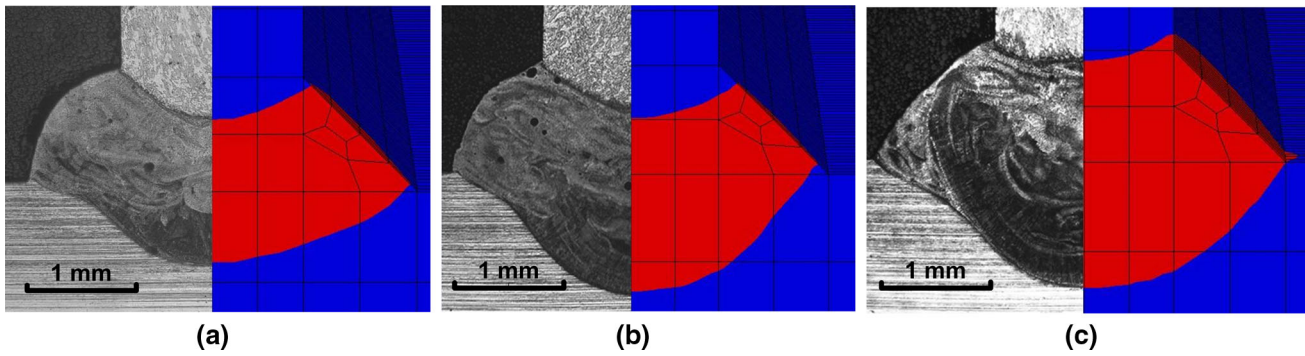
Fig. 7—Comparison of the fusion boundary of laser welding processes at different power: (a) 1400 W, (b) 1700 W, and (c) 2000 W.
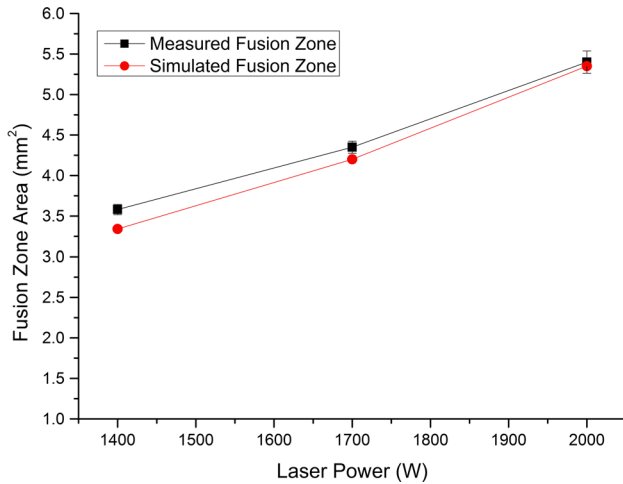

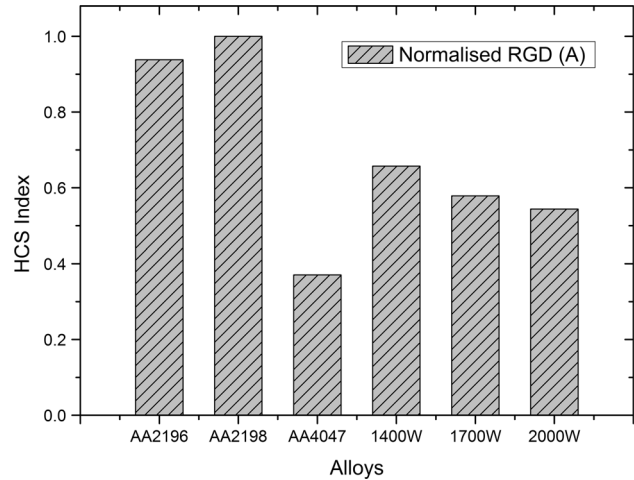Fig. 8—Comparison of the fusion zone area of laser welding processes at different powers.

Fig. 9—The normalized HCS integral A corresponding to the parent metal, filler wire, and the weld mixtures at various laser powers.

B. HCS Modeling Results and Discussion

The hot cracking susceptibility for the three weld powers used in this study was predicted using the two-level RDG criteria, as described previously. To calculate the average melt pool composition, it was assumed that the skin material AA2198, stringer AA2196, and filler wire AA4047 were perfectly mixed in the fusion zone. The melt pool composition can then simply be calculated by taking a weighted average of the three component materials scaled according to the fraction of each in the melt. Varying welding parameters will produce different proportions of skin, stringer, and filler materials, therefore resulting in different composition in the final mixed fusion zone. As shown in Figure 7, the cross-sectional area of the fusion zone consists of melted skin, stringer, and additional filler material.

The calculated compositions of the mixed fusion zone as a function of laser powers are listed in Table VI. Because the filler wire was added into the weld at constant speed regardless of the change of laser power, more parent materials were melted into the fusion zone with an increase in laser power, so that the concentration of Cu increases while that of Si decreases. The solid fraction for each melt pool composition as a function of temperature during solidification was calculated and used to calculate the A and B parameters in the HCS model. The calculated A parameter (normalized value) is shown in Figure 9 for the mixed fusion zone, and for the parent and filler materials. The integral B varies in a very similar way and so is not shown. It can be seen that as expected, the relative hot cracking susceptibility (A parameter) of the parent materials AA2198 and AA2196 are very high suggesting a potential hot cracking problem in lithium-bearing alloys. This is largely a

Table VI. Composition of Fusion Zone at Different Laser Powers by Assuming Perfect Mixing (Weight Percent)

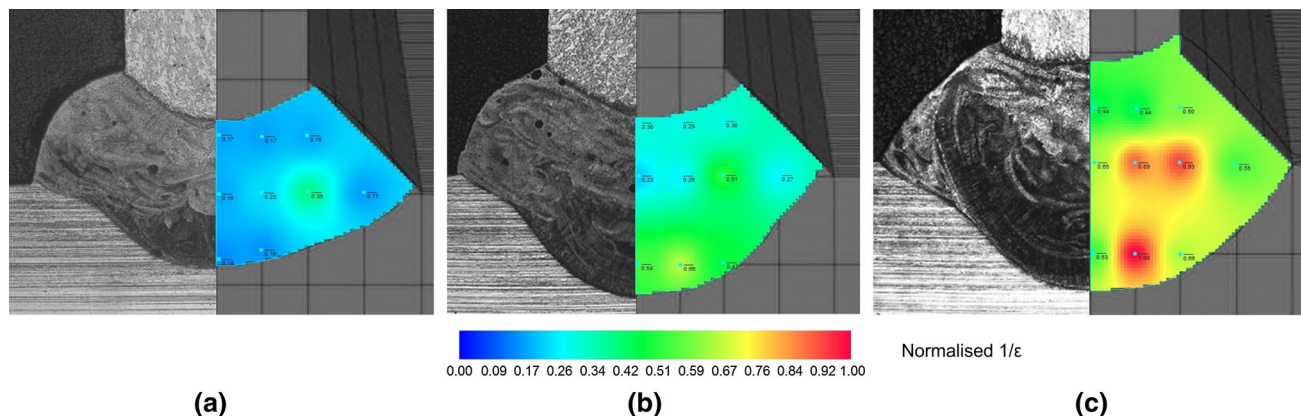| Power	AA4047 Percentage	Si	Fe	Cu	Mn	Mg	Cr	Zn	Ti	Ag	Li	Zr	Al
1400 W	35.5	4.28	0.32	2.17	0.16	0.25	0.02	0.08	0.01	0.09	0.85	0.08	bal.
1700 W	29.2	3.52	0.27	2.39	0.13	0.26	0.03	0.07	0.01	0.13	0.86	0.09	bal.
2000 W	25.2	3.04	0.24	2.49	0.14	0.27	0.03	0.07	0.01	0.13	0.94	0.1	bal.

Fig. 10—The normalized HCS index based on the maximum strain rate can be sustained by the weld obtained through various laser powers: (a) 1400 W, (b) 1700 W, and (c) 2000 W (Color figure online).

result of the wide freezing range in these materials (a common feature of all high-strength age hardenable aluminum alloys).[1]

In contrast, as expected, the AA4047 filler material shows a very low hot cracking susceptibility. The normalized HCS index of the mixed weld compositions lies between the parent and filler materials indicating the Si-rich filler wire can effectively reduce the hot cracking susceptibility of the parent metals. It can also be seen that according to the first-level RDG criterion (A parameter evaluation), the HCS of the mixture of alloys in the weld decreases slightly with increasing laser power from 1400 to 2000 W. This is initially surprising, since the high powered weld has the lowest proportion of filler compared to parent material. This point is explored in more detail later.

Predictions based on the more complex second-level RDG criterion were also made. As discussed, this criterion considers not only the melt pool composition but also the weld thermal field. Based on the previous finite element modeling results, the steady-state thermal field data for different welding powers were extracted and used as input for the second-level HCS index calculation. The thermal gradient G at the nodal positions on the weld cross section was obtained from the thermal model. For a weld power of 1400 W, there were 9 nodal positions included in the fusion zone, while there were 10 nodal positions for both 1700 and 2000 W conditions, since the fusion zone was larger. The maximum strain rates sustainable by the weld material obtained under various laser powers were calculated using Eq. [7] and the inverse of this parameter gives the relative HCS index according to the second-level RDG criterion. Figure 10 plots the normalized second-level HCS index on the cross section of the fusion zone for different weld powers. The calculation shows that the fusion zone obtained at higher laser power can sustain a smaller strain rate therefore is more likely to initiate hot cracking. Note that this is exactly opposite to the trend in HCS with weld power estimated based on the A parameter alone.

The first-level RDG criterion is solely based on the solidification range of the mixed alloys and not the local
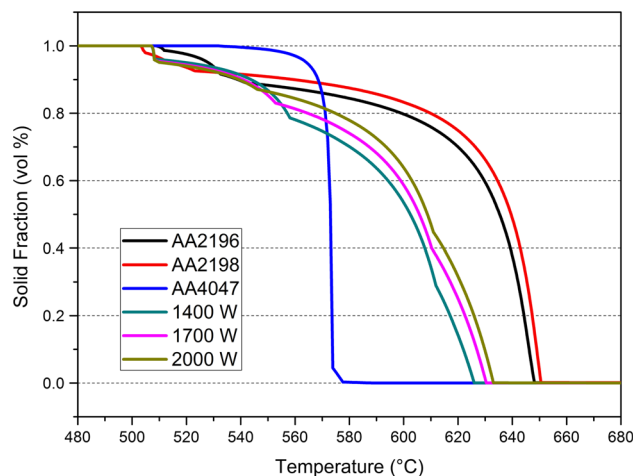

Fig. 11—Solidification phase of the AA2198, AA2196, AA4047 and the mixed alloys in fusion zones (Color figure online).

thermal conditions. Figure 11 depicts the solidification path of the AA2198, AA2196, AA4047 and the mixed alloy compositions obtained in the fusion zone for different welding parameters. The integral (A parameter) is the area bounded by the solidification curve between the coherency temperature and liquidus temperature. It can be seen that the AA2198 and AA2196 have the widest solidification temperature range from solidus to liquidus and therefore have the largest RDG integral (A). In contrast, AA4047 has a significantly smaller solidification temperature range and thus much smaller HCS index. By adding the Si-rich filler wire into the weld, the liquidus of the mixed compositions is significantly reduced, resulting in a strong reduction in the HCS predicted on the basis of the A parameter.

As suggested by Rappaz,[5] the end of the solidification is particularly important as inter-dendritic bridging occurs in this region. A zoom-in of the later stage of the solidification path is plotted in Figure 12. It can be seen that, at the beginning stage of solidification, the mixed alloy obtained for 1400 W laser power has a relatively low liquidus temperature. However, in this case, final solidification (from 0.8 to 1 solid fraction) takes place

over a wider temperature range than in the other cases, leading to a larger A parameter and higher predicted HCS. This indicates that although in general the HCS of two Al-Li alloys in this study can be significantly reduced by introducing substantial proportions of Si (Table VI), within the regime of the mixtures, the HCS index does not decrease simply by increasing the Si content. Similar results have also been reported by Drezet.[19]

In order to investigate the effects of Si and Cu, which are the main elements affecting the A parameter in the weld mixture, calculations were carried out by varying Si and Cu content respectively while keeping the other elements fixed at the same level as the mixture obtained by 1700 W laser power, as listed in Table VII. The composition level from 1700 W laser power was chosen because it provided an average reference of the weld mixture. As plotted in Figure 13, it can be seen that the HCS peaks at Si = 0.4 pct or Cu = 1.2 pct, respectively and decreases with further increase of either element. As listed in Table VI, when the laser power increases from 1400 to 2000 W, the content of Si decreases from 4.3 to 3.0 pct while the concentration of Cu increases from 2.2 to 2.5 pct.

As indicated by the 'A' curves in Figure 13, 2-4 pct of Si introduced into the weld would be expected to produce a low HCS in the Al-Cu-Li-x alloy system (Table VII) and further small changes in Si concentration have very little influence on the integral A. However, an increase of Cu from 2.2 to 2.5 pct results in a larger reduction in A parameter, compared with the small increase caused by the reduction of Si from 4.3 to 3.0 pct (as indicated by the red and black arrows in

Figure 13). In this case, an increase in Cu acts to reduce the A parameter more strongly than the decrease in Si increases it. This results in the prediction that, as more parent material is introduced into the melt pool (i.e., by use of higher welding power), the A parameter and hence HCS (according to the first-level RDG criterion) will be reduced.

The second-level RDG criterion considers both alloy composition and the process, and should provide a more accurate assessment of hot cracking susceptibility than the first-level criterion. As illustrated in Eq. [7], the first term is the maximum strain rate that can be provided by the liquid metal flowing into the bottom of the dendritic network, which depends on the cavitation pressure, the secondary arm spacing, thermal gradient, and liquid viscosity. The second term is the strain rate required to accommodate the shrinkage during the liquid-to-solid phase transformation. Therefore, the $\dot{\varepsilon}_{p,max}$ shows the capacity of the mushy zone to accommodate the mechanical strain rate induced by the shrinkage of the solid underneath upon further cooling. The bigger the 'spare' strain rate capacity $\dot{\varepsilon}_{p,max}$, the larger the mechanical strain rate can be tolerated, so the lower the risk of hot cracking at the end of solidification. The HCS is hence proportional to the inverse of the maximum strain rate, i.e., proportional to $1/\dot{\varepsilon}_{p,max}$.

For second-level HCS modeling, when the laser power increased from 1400 to 2000 W, the thermal gradient in the fusion zone increased correspondingly. The secondary dendrite arm spacing λ_2 is inversely affected by the cooling rate, which directly relates to the thermal gradient. Hence, the secondary dendrite arm spacing decreased with increasing laser power. As can be seen in
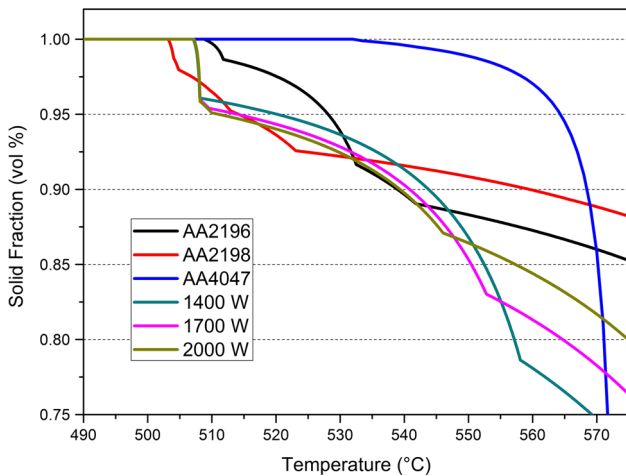

Fig. 12—Zoom at the solid fractions higher than 75 pct of the solidification phase (Color figure online).
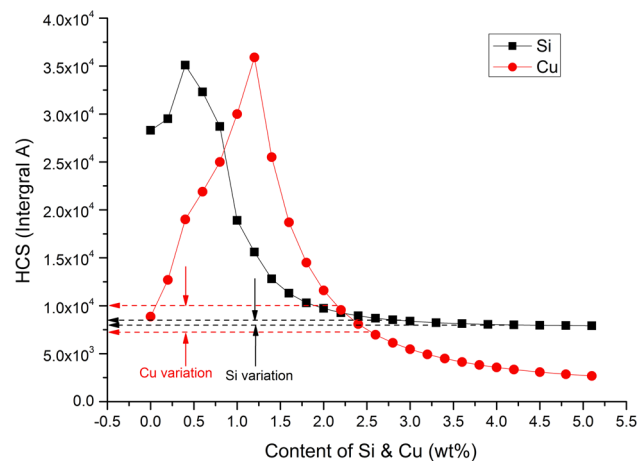

Fig. 13—Influences of Si and Cu on the HCS of the weld mixture on the basis of 1700W laser welding power.

Table VII. Compositions for Calculating the Influences of Si and Cu on the A Parameter (Weight Percent)

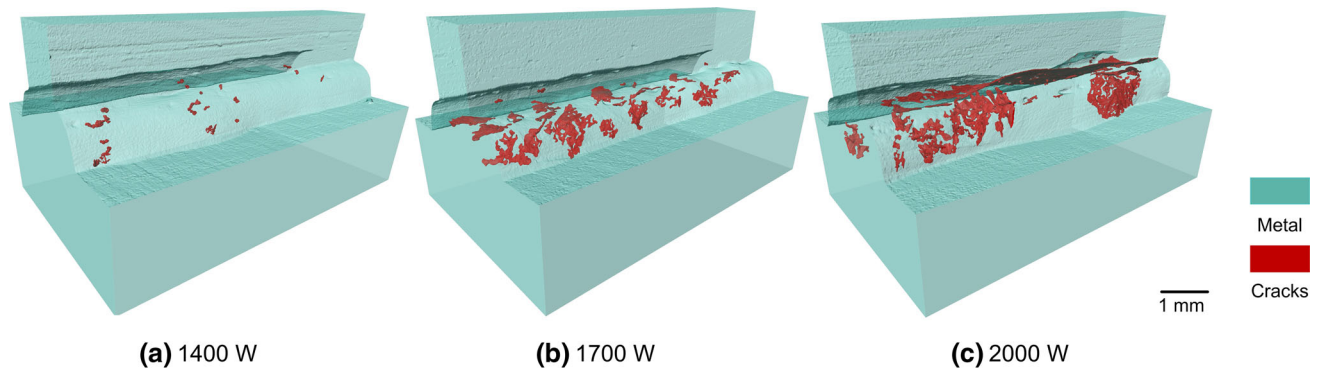|	Si	Cu	Fe	Mn	Mg	Cr	Zn	Ti	Ag	Li	Zr	Al
1	varies between 0 and 5.1	2.39	0.27	0.13	0.26	0.03	0.07	0.01	0.13	0.86	0.09	bal.
2	3.52	varies between 0 and 5.1	0.27	0.13	0.26	0.03	0.07	0.01	0.13	0.86	0.09	bal.

(a) 1400 W   **(b)** 1700 W   **(c)** 2000 W

Fig. 14—Visualization of X-ray tomography results reveal the cracks inside the welds obtained through various laser welding powers: (*a*) 1400 W, (*b*) 1700 W, and (*c*) 2000 W (Color figure online).

the expression of the first term in Eq. [7], the effect of increases in the thermal gradient will be outweighed by the reduced secondary arm spacing, on which there is a squared dependence. Therefore, with an increase of laser power, the strain rate sustainable in the weld is predicted to become smaller, indicating a larger hot cracking susceptibility. It was also noticed that the HCS index was uneven in the fusion zone and it is therefore predicted that there will be regions of the weld more susceptible to cracking (greater HCS) regardless of weld power (Figure 10) due to variations in the thermal field. In practice, variations in melt pool composition caused by imperfect mixing (which is ignored in the present model) may also produce a significant local variation in HCS.

In order to test the predictions of the RDG model, welds made with various powers were examined by XCT to reveal cracks and porosity. During the segmentation and visualization process, features having near-spherical shape were treated as porosity and separated from cracks, which had relatively larger aspect ratios. Figure 14 shows the distribution of cracks in the welds. The results clearly show that the population of cracks increases with increasing laser power, which is in line with the HCS modeling predictions according to the second-level RDG criterion. However, the 'hot spots' of hot cracking shown in the modeling results cannot be directly linked to the experimental results. This is because cracking in the real weld is also influenced by other complex phenomena that are not included in the modeling framework. For example, as indicated in Figure 15, the radiograph of cross-sectional view of the weld made with a power of 2000 W, it was found that relatively big gas bubbles were gathered close to the upper fusion boundary. The gas bubbles formed during the welding process tend to float upwards due to the buoyancy force in the liquid metal. These bubbles are then stopped by the stringer and cannot escape from the melt pool. This porosity is likely to promote severe hot cracking, which is not considered by either the first- or second-order RDG models for HCS used here.

On the basis of the above discussion, the first-level RDG criterion is sufficient to justify the benefits of adding Si-rich filler wire into the Al-Li alloy welds, however, it is not capable of distinguishing the variation
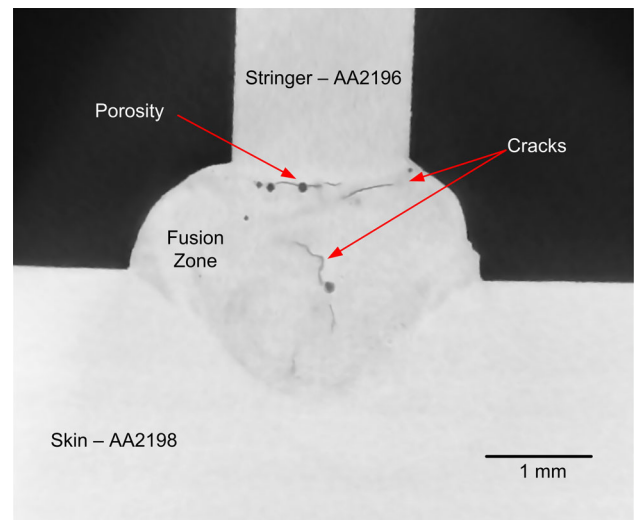

Fig. 15—Ortho slice of XCT cross-sectional view of weld obtained through 2000 W laser.

brought by the small changes in welding power. Indeed, by applying the first-level RDG criterion, which depends only on the composition of the fusion zone, it would be predicted that a higher weld power should produce fewer defects, whereas the opposite was observed. The second-level RDG criterion, which also includes the effects of the thermal field and microstructure (secondary arm spacing), predicts the opposite trend: welds produced at higher power will be more susceptible to hot cracking and this agrees with the observations. This trend of increasing hot crack susceptibility at increasing weld power is consistent with previous studies on other aluminum alloy systems.[20] It should be noted that neither the first nor the second level of RDG criterion can determine whether the weld will or will not actually crack at the end of solidification. It only gives relative indication of the likelihood of hot cracking. Also, it can only be used as an indicator of the initiation, rather than predict the length or propagation of the hot crack. To make a final decision of the optimized welding parameters, other factors such as weld surface morphology, welding efficiency, and mechanical properties still need to be considered. However, the present model still

provides a useful tool to aid selection of likely suitable process parameters and filler material, and provides a physics-based framework to determine these parameters rather than the usual entirely empirical approach.

V. CONCLUSIONS

In summary, a coupled model has been developed and validated for assessing the hot cracking susceptibility (HCS) of an Al-Li alloy structure during dual-beam laser welding processes. The finite element process model was able to simulate the thermal history the welds have experienced and provide the input parameters needed for the prediction of HCS. The HCS model has been developed through adapting an existing model developed by Rappaz, Drezet, and Gremaud (RDG) for prediction of cracking during casting. The RDG model can be used at two levels of complexity. At the first level, the prediction depends only on the melt pool composition during welding. It was demonstrated that at this level, the model correctly predicts the beneficial effect of using a Si-rich filler material, but predicts the wrong trend between weld power and HCS. Only using the second-level RDG model, which also includes the thermal history, can the correct trend between increasing weld power and increasing HCS be captured.

X-ray tomography reveals that in addition to hot cracks, which are predicted by the present model, the welds can contain other defects in the form of gas porosity. The model framework presented here does not predict such porosity, but this would be required for a complete prediction of weld integrity. Nevertheless, the model developed here provides a useful tool in guiding weld process and filler selection, as well as helping in understanding the factors that contribute to HCS. Although applied to the specific case of laser welding of Al-Li alloys, the model methodology could readily be adapted to other welding processes and aluminum alloy classes.

REFERENCES

1. A. Kostrivas and J.C. Lippold: *Int. Mater. Rev.*, 1999, vol. 44, p. 217.
2. J.R. Pickens: *J. Mater. Sci.*, 1990, vol. 25, p. 3035.
3. P.A. Molian and T.S. Srivatsan: *J. Mater. Sci.*, 1990, vol. 25, p. 3347.
4. J.R. Pickens: *J. Mater. Sci.*, 1985, vol. 20, p. 4247.
5. M. Rappaz, J.-M. Drezet, and M. Gremaud: *Metall. Mater. Trans. A*, 1999, vol. 30A, p. 449.
6. S. Kou: *Acta Mater.*, 2015, vol. 88, p. 366.
7. N. Coniglio and C.E. Cross: *Metall. Mater. Trans. A*, 2009, vol. 40A, p. 2718.
8. L. Sweet, M.A. Easton, J.A. Taylor, J.F. Grandfield, C.J. Davidson, L. Lu, M.J. Couper, and D.H. StJohn: *Metall. Mater. Trans. A*, 2012, vol. 44A, p. 5396.
9. M.A. Easton, H. Wang, J. Grandfield, C.J. Davidson, D.H. StJohn, L.D. Sweet, and M.J. Couper: *Metall. Mater. Trans. A*, 2012, vol. 43A, p. 3227.
10. N. Hatami, R. Babaei, M. Dadashzadeh, and P. Davami: *J. Mater. Process. Technol.*, 2008, vol. 205, p. 506.
11. J.-M. Drezet, M. S.-F. Lima, J.-D. Wagniere, M. Rappaz, and W. Kurz, in *Invit. Lect. 61st Inter. Conf. Inter. Inst. Weld.* (Graz, Italy, 2008).
12. J. Goldak, A. Chakravarti, and M. Bibby: *Metall. Trans. B*, 1984, vol. 15, p. 299.
13. A. Lundbäck and H. Runnemalm: *Sci. Technol. Weld. Join.*, 2005, vol. 10, p. 717.
14. A. Larsen, M. Stolpe, and J.H. Hattel: *Eng. Comput.*, 2012, vol. 29, p. 65.
15. D.G. Eskin and L. Katgerman: *Metall. Mater. Trans. A*, 2007, vol. 38A, p. 1511.
16. T. Clyne and G. Davies: *Br. Foundrym.*, 1981, vol. 74, p. 65.
17. W. Kurz and D.J. Fisher: *Fundamentals of Solidification*, 3rd ed., Trans Tech, Switzerland, 1992.
18. Z. Guo, N. Saunders, A.P. Miodownik, and J.P. Schille, in *Proc. 7th Pacific Rim Int. Conf. Model. Cast. Solidif. Process.* (Dalian, China, 2007), pp. 19–22.
19. J.-M. Drezet and D. Allehaux, in *Hot Crack. Phenom. Welds II* (2008), pp. 19–37.
20. G. Mathers: *The Welding of Aluminium and Its Alloys*, Woodhead Publishing Ltd, Cambridge, 2002.